Nanoscale

Accepted Manuscript

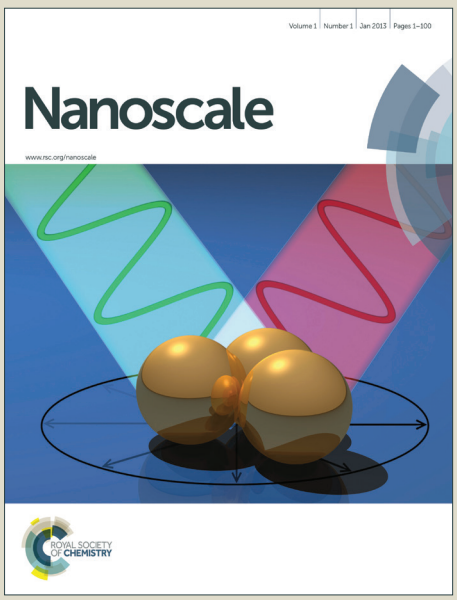

ROYAL SOCIETY OF CHEMISTRY

www.rsc.org/nanoscale

Well-defined hollow nanochanneled-silica nanosphere prepared with aids of sacrificial copolymer nanosphere and surfactant nanocylinders†

Young Yong Kim,[+a] Bora Hwang,[+b] Sungjin Song,[a] Brian J. Ree,[a] Yongjin Kim,[a] Seo Yeon Cho,[b] Kyuyoung Heo,[a] Yong Ku Kwon*[b] and Moonhor Ree*[a]

Abstract: A new approach for synthesizing well-defined hollow nanochanneled-silica nanosphere particles is demonstrated, and the structural details of these particles are described for the first time. Positively charged styrene copolymer nanospheres with a clean, smooth surface and a very narrow size distribution are synthesized by surfactant-free emulsion copolymerization and used as a thermally sacrificial core template for the production of core–shell nanoparticles. A surfactant/silica composite shell with a uniform thickness is successfully produced and deposited onto the polymeric core template by charge density matching between the polymer nanosphere template surface and the negatively charged silica precursors and then followed by selective thermal decomposition of the polymeric core and the surfactant cylinder domains in the shell, producing the hollow nanochanneled-silica nanosphere. Comprehensive, quantitative structural analyses collectively confirm that the obtained nanoparticles are structurally well defined with a hollow core and a shell composed of cylindrical nanochannels that provide facile accessibility to the hollow interior space. Overall, the hollow nanochanneled-silica nanoparticles have great potential for applications in various fields.

Key Words: monodisperse, hollow nanochanneled-silica nanosphere, surfactant-free emulsion copolymerization, charged polymeric nanosphere, shell deposition assisted with charge density matching, quantitative structural analysis

[a]*Division of Advanced Materials Science, Department of Chemistry, Pohang Accelerator Laboratory, Polymer Research Institute, and BK School of Molecular Science, Pohang University of Science & Technology, Pohang 790-784, Korea. E-mail: ree@postech.edu; Fax: +82-54-279-2120; Tel: +82-54-279-3399*

[b]*Department of Polymer Science and Engineering, Inha University, 253 Yonghyun-Dong, Nam-Gu, Incheon 402-751, Republic of Korea. E-mail: ykkwon@inha.ac.kr; Fax: +82-32-865-5178; Tel: +82-32-860-7482*

† Electronic supplementary information (ESI) available: SXS data analysis, GIXS data analysis, GPC data, SXS data and GIXS data are available.

+ Y. Y. Kim ad B. Hwang contributed equally to this work.

Introduction

Porous particles, as well as hollow particles (i.e., capsules), have inherently large surface areas as well as easily tunable chemical and physical properties.[1-8] Due to such advantages, they have garnered great interest in academia and industry for potential applications in various fields such as catalysis, selective separation, gas adsorption, drug and gene delivery, biomedical imaging, cosmetics, photonics, photovoltaics, rechargeable batteries, and sensors.[4-6,8-17] As a result of extensive research, various porous and hollow particle systems have been reported.

Porous particles, however, have a limited interior space due to the nature of their structures and thus often face to need a relatively large space for the desired chemical species in some applications, such as drug and gene deliveries. On the other hand, a challenging aspect for applications using hollow particles is providing sufficiently facile access to the hollow interior space for appropriate releasing and refilling of the chemical species. An approach to solve these limitations is to mold the porous characteristics and the hollow feature into one particle system. Based on this idea, much research effort has been devoted to the synthesis of hollow porous particles. As a result, several hollow porous particles, in particular hollow mesoporous particles, have been reported.[4-12,14-18]

Nevertheless, these particles very often displayed a broad distribution of overall size and/or shell thickness rather than being uniform. Furthermore, in each case the particles' morphology and size distribution were not investigated in detail. In particular, their shell morphology, knowledge of which is critical for effective application of hollow porous particles, is not fully understood. Therefore, preparing hollow porous particles with well-defined structural features (e.g., the size of the hollow space as well as the thickness and pore structure of the shell) is still challenging, yet remains important for these particles to be applied with high performance in the various fields mentioned above.

In this study, we sought to develop a novel method for preparing well-defined hollow nanochanneled-silica nanospheres, and to quantitatively characterize their nanostructures. Positively charged poly(styrene-*co*-butyl acrylate-*co*-2-[(methacryloxy)ethyl]trimethyl ammonium chloride) (PSBM) nanoparticles were successfully synthesized without any bridging flocculation and

secondary nucleation by surfactant-free emulsion copolymerization. Excitingly the PSBM particles were spherical and had a very clean, smooth surface as well as a well-defined size in a very narrow distribution. Onto the individual PSBM nanospheres, a surfactant/silica composite shell with a uniform thickness was deposited in a controlled manner by the hydrolysis polycondensation of tetraethylorthosilicate (TEOS) combined together with the self-assembly of cetyltrimethylammonium bromide (CTAB) surfactant. The PSBM core and the CTAB self-assemblies in the core-shell particles were selectively removed out without collapse by sacrificial thermal degradation, producing stable, well-defined hollow nanochanneled-silica nanospheres. Overall, this study demonstrated for the first time the synthesis and structural details of monodisperse, stable, well-defined hollow nanochanneled-silica nanosphere particles.

Experimental

Materials

All chemicals used in this study were purchased from Sigma-Aldrich (St. Paul, MN, USA): styrene (St, >99% purity), butyl acrylate (BA, >99% purity), 2-[(methacryloxy)ethyl]trimethyl ammonium chloride (MOTAC, 75 wt% in water), α,α'-azodiisobutyramidine dihydrochloride (AIBA, 97%), TEOS, CTAB ($C_{16}H_{13}(CH_3)_3NBr$), and ethanol. AIBA was purified by recrystallization from a water/acetone mixture (50/50, wt/wt) before use. Styrene was purified with sodium hydroxide (NaOH) solution to remove inhibitors. Other reagents were used without further purification.

Synthesis

Hollow nanochanneled-silica particles were synthesized in a three-step manner, as shown in Scheme 1. PSBM nanoparticles were synthesized by surfactant-free emulsion polymerization, according to a method reported prevoulsly.[8] The surfactant-free emulsion copolymerization of St (15.000 g, 0.144), BA (1.000 g) and MOTAC (0.100 g) was carried out in deionized, distilled water (150 mL) at 70 °C for 8 h, with the aid of the AIBA initiator (0.250 g); the reaction medium was stirred with a speed of 700 rpm through the whole copolymerization process. Thereafter, the synthesized polymeric particles were purified by three cycles of centrifugation and redispersion in the deionized, distilled water, and followed by freeze drying, producing the target PSBM particles.

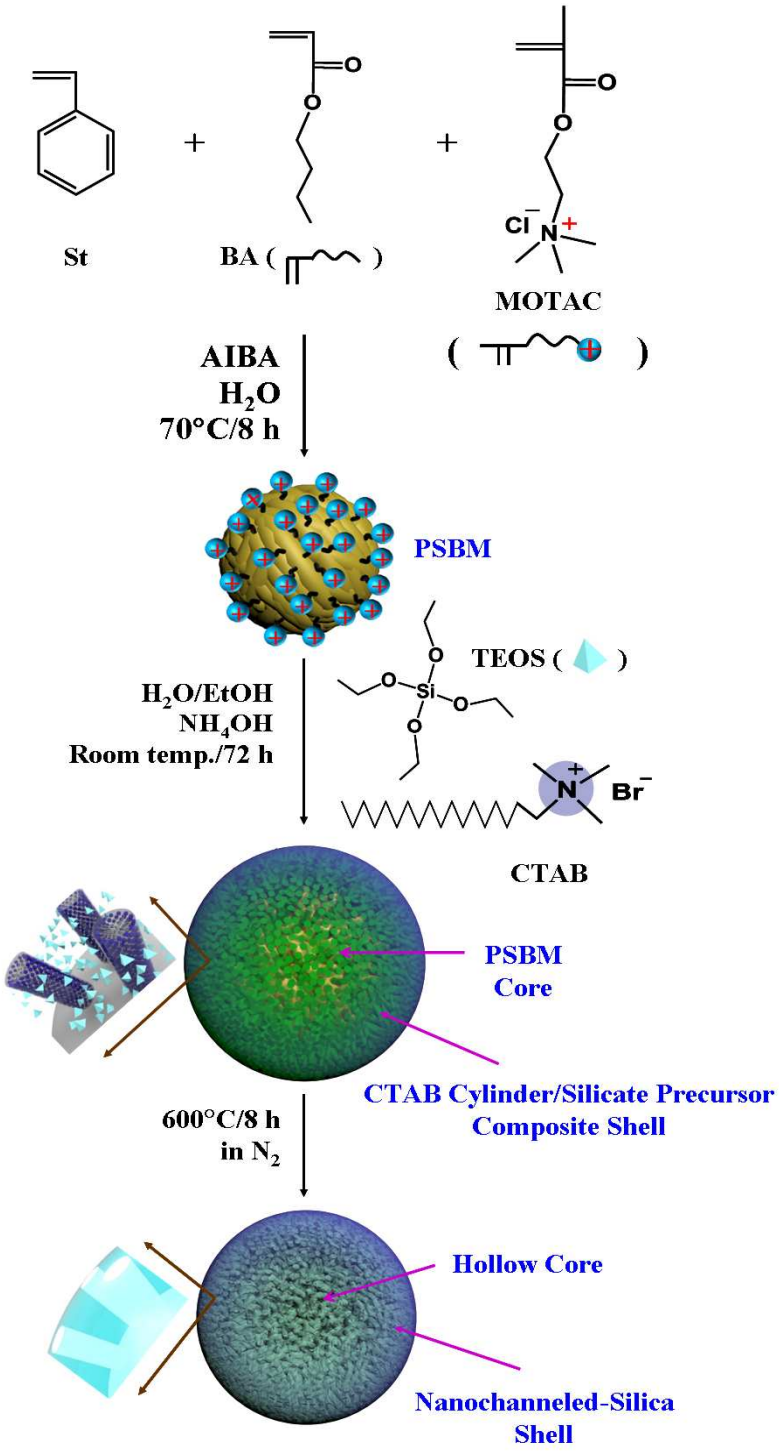

Scheme 1 Synthetic route for core-shell particle and its hollow nanochanneled-silica nanoparticle.

The obtained PSBM particles (0.500 g) were dispersed in deionized, distilled water (51 mL).

Then, CTAB (0.800 g), ammonium hydroxide (1.0 mL), and ethanol (21 mL) were added and followed by stirring for 30 min. Subsequently, TEOS (1.5 mL) was added dropwise with stirring at room temperature. The mixture was further stirred at room temperature for 72 h. The resulting reaction mixture was centrifuged, washed twice with ethanol and water, and then freeze-dried for 48 h, producing PSBM core-silica/CTAB shell particles. The obtained core-shell particles were further subjected to thermal treatment at 600 °C under nitrogen atmosphere for 8 h in order to selectively calcine out the PSBM core and the CTAM component in the shell part.

Measurements

Nuclear magnetic resonance (NMR) spectroscopy measurements were carried out using a Bruker NMR spectrometer (model AV500 FT-NMR, Rheinstetten, BW, Germany) with proton (^{1}H) and carbon (^{13}C) probes. Infrared (IR) spectroscopy analysis was performed using an IR spectrometer (model Research Series 2, ATI Mattson, Lakewood, NJ, USA). Molecular weight measurements were conducted using a gel permeation chromatography (GPC; model PL-GPC 210, Polymer Labs, Amherst, MA, USA) equipped with a set of gel columns (3 columns of PL Gel Mixed-E). The GPC system was calibrated with polystyrene standards. GPC runs were carried out with a flow rate of 0.6 mL/min at 25 °C using tetrahydrofuran (THF) as an eluent; GPC chromatograms were recorded by a Shodex refractive index (RI) detector (model RI-101, Shoko Scientific, Yokohama, Japan).

Thermogravimetric analysis (TGA) was carried out at a scan rate of 10.0 °C/min under nitrogen atmosphere using a Thermal Analyzer (model Q50, New Castle, DE, USA). Scanning electron microscopy (SEM) analysis was conducted using a Hitachi instrument (model S-4200, Tokyo, Japan), whereas tansmission electron microscopy (TEM) analysis was performed using a Philips instrument (model CM-220, Eindhoven, Netherlands). Brunauer-Emmet-Teller (BET) analysis was carried out using a surface area analyzer (model TriStar 3000, Micromeritics, Norcross, GA, USA).

Solution X-ray scattering (SXS) measurements were conducted at the 9A beamline[19-21] of the Pohang Accelerator Laboratory (PAL) at Pohang University of Science & Technology (POSTECH). Each nanoparticle sample was dispersed in ethanol, producing a solution with a concentration of 0.5−1.0 wt%. The obtained nanoparticle solutions were used for solution X-ray scattering analysis. An X-ray beam with a wavelength λ of 0.1100 nm was used. The X-ray beam size at the sample

stage was 150 × 350 μm^2. A two dimensional (2D) charge-coupled detector (CCD) (model 2D MAR, Rayonix, Evanston, IL, USA) was employed. Sample-to-detector distances (SDD) of 300 and 6500 mm were used. The scattering angle was calibrated with silver behenate and poly(styrene-*b*-ethylene-*b*-butadiene-*b*-styrene) standards. We used solution sample cells with mica windows 10 μm in thickness, a volume of 50 μL, and X-ray beam path length of 0.7 mm. All scattering measurements were carried out at 25 °C. The scattering data collection was performed for 60 s. Each measured 2D scattering pattern was circularly averaged from the beam center, normalized to the transmitted X-ray beam intensity (monitored with a scintillation counter placed behind the sample cell), and corrected for scattering arising from the ethanol solvent.

Grazing Incidence X-Ray Scattering (GIXS) measurements were carried out at the 3C and 9A beamlines[22-25] of PAL. The solution (1.0 wt%) in ethanol of each nanoparticle sample was spin-casted on silicon substrates at 200 rpm for 30 s and then followed by drying in air ambient at room temperature for 6 h. The samples were measured in vacuum at room temperature. SDD = 300 mm and 3000 mm. Scattering data collection time was 30–60 s with synchrotron X-ray radiation sources (λ = 0.118 nm at the 3C beamline and λ = 0.110 nm at the 9A beamline) using a Mar CCD. The incidence angle α_i of the X-ray beam was varied in the range of 0.140–0.146°, which is between the critical angles of the nanoparticle samples and the silicon substrates. The scattering angles were corrected according to the reflected beam position with changing incidence angle and with respect to pre-calibrated polystyrene-*b*-polyethylene-*b*-polybutadiene-*b*-polystyrene block copolymer and silver behenate powder (TCI, Tokyo, Japan). Aluminum foil pieces were employed as a semitransparent beam stop because the intensity of the specular reflection from silicon substrate is much stronger than that of GIXS near the critical angle.

In addition, X-ray reflectivity (XR) analysis was further conducted with an X-ray beam (λ = 0.1240 nm) in θ–2θ scanning mode at the 3D beamline[26,27] of PAL using a Huber four-circle goniometer equipped with a scintillation counter (model EDR, Bede Scientific, Centennial, CO, USA). In measurements the reflected beam intensity was normalized by the primary beam intensity that was measured using an ionization chamber.

Results and discussion

We synthesized hollow mesoporous-silica nanoparticles in three-step reactions, as shown in Scheme 1. In the first stage, positively charged PSBM particles were synthesized by the surfactant-free emulsion copolymerization of St, BA and MOTAC in water with the aid of the AIBA initiator. This method could produce monodisperse nanospheres with clear surfaces, because it avoids the use of surfactants during polymerization. Instead, the ionic initiator, AIBA, and the ionogenic comonomer, MOTAC were added to improve the stability of the polymer colloids. Unlike conventional emulsion polymerizations, both homogeneous and micellar nucleation are likely to occur in soap-free emulsion polymerization. Some of the obtained PSBM particles were dissolved in deuterated chloroform ($CDCl_3$) and then examined by ^1H and ^{13}C NMR spectroscopies. The obtained chemical shifts were assigned as follows (Fig. 1a and b). ^1H NMR (500 MHz, $CDCl_3$, δ (ppm)): 7.04–7.09 (br, 158H, aromatic proton), 6.35–6.80 (br, 105H, aromatic proton), 3.28–3.79 (br, 9H, -N(CH_3)$_3$), 1.05–2.22 (br, 190H, backbone), 0.77–0.92 (br, 11H, methyl group of BA); ^{13}C NMR (125 MHz, $CDCl_3$, δ (ppm)): 145.2 (acrylate, -*C*OO-), 127.9 (aromatic carbon of phenyl group), 40.4 (three methyl group of MOTAC –N(*C*H_3)$_3$). The chemical composition of PSBM was estimated to have an average molar ratio of 35.0 St units, 3.5 BA units and 1.0 MOTAC unit from the integrated areas of the characteristic shifts at 6.35–7.09 ppm (St unit), 3.28–3.79 ppm (MOTAC unit) and 0.77–0.92 ppm (BA unit). The determined chemical composition was found to be different from the molar feed ratio of the monomers initially loaded in the surfactant-free emulsion copolymerization. The PSBM particles were additionally examined in pellets by IR spectroscopy. The PSBM particle revealed aromatic C–H stretching peak around 3000-3100 cm^{-1}, aromatic C–C stretching band at 1470 cm^{-1}, vibrational characteristic peak of mono-substituted phenyl groups at 690 and 750 cm^{-1} of the St unit, C=O stretching band at 1740 cm^{-1} and C-O-C stretching peak at 1150 cm^{-1} of the BA and MOTAC units, and aliphatic C-H stretch band at 2800-3000 cm^{-1}, as shown Fig. 2a. Another part of the PSBM particles was dissolved in THF for a molecular weight analysis using GPC; a representative of the measured GPC traces is given in ESI Fig. S1.† The GPC analysis found that the

PSBM particle has a number-average molecular weight $\overline{M_n}$ of 51800 and a polydispersity index PDI (= $\overline{M_w}/\overline{M_n}$; $\overline{M_w}$, weight-average molecular weight) of 3.001. These NMR, IR and GPC analysis results collectively confirm that the PSBM particle was successfully synthesized with a reasonably high molecular weight.

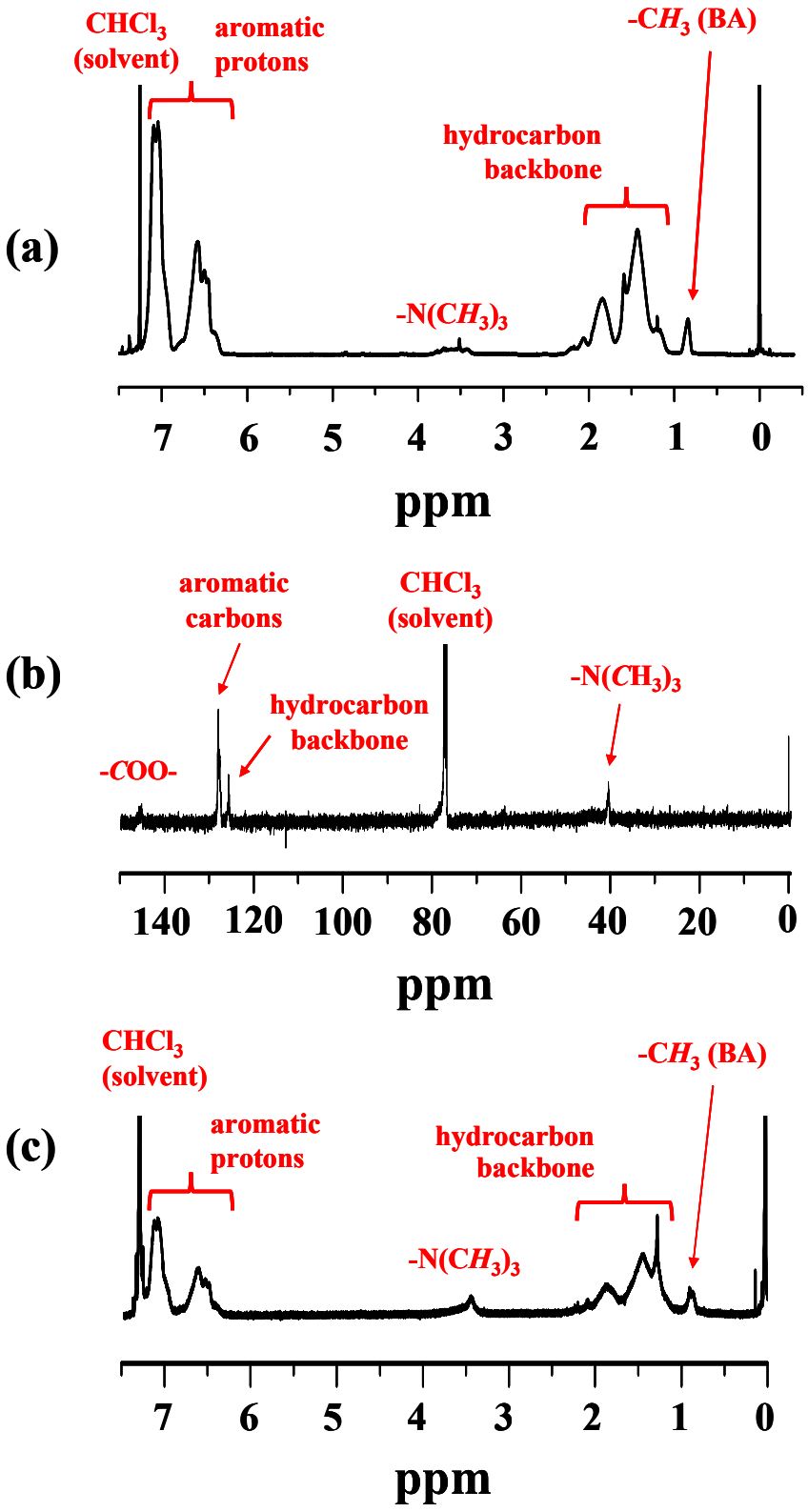

Fig. 1 NMR spectra of PSBM and its core-shell particle measured in $CDCl_3$: (a) ^1H NMR, PSBM molecules dissolved in the solvent; (b) ^{13}C NMR, PSBM molecules dissolved in the solvent; (c) ^1H NMR, PSBM core-silica precursor/CTAB composite shell particles dispersed in the solvent.

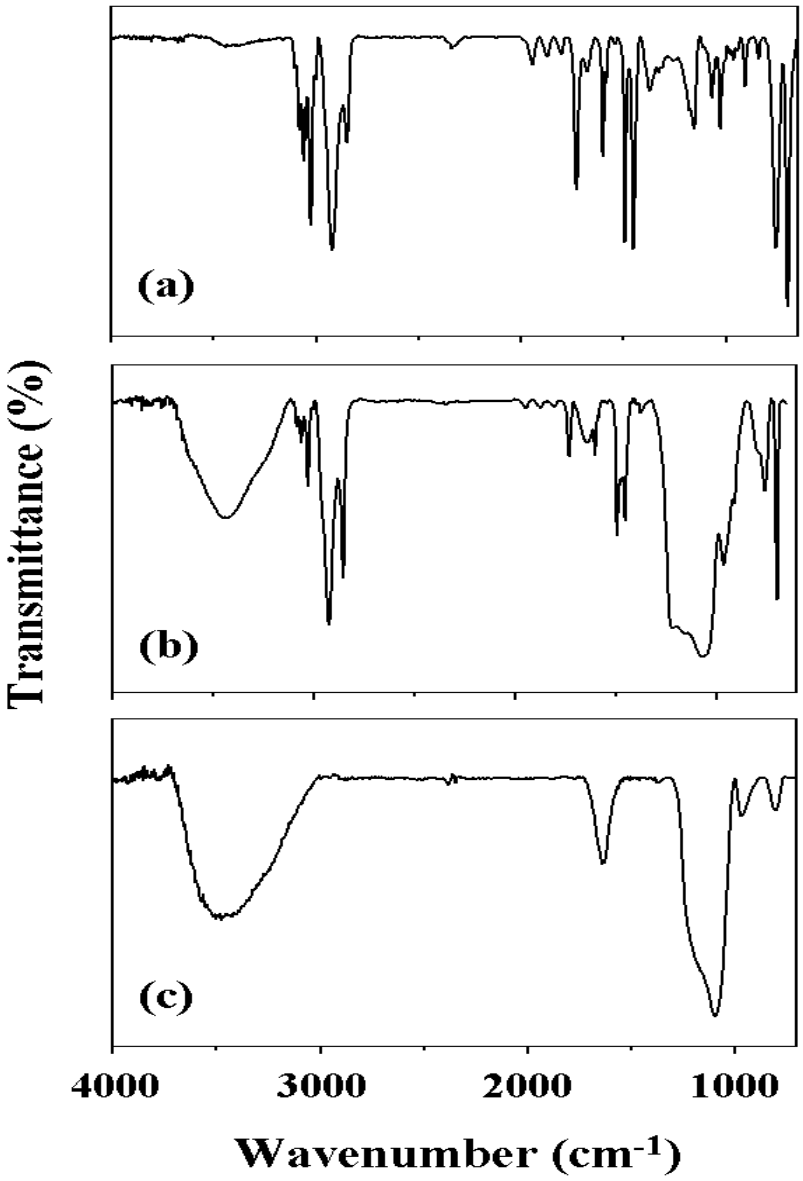

Fig. 2 IR spectra were measured in pellets: (a) PSBM particle; (b) PSBM core-silica precursor/CTAB composite shell particle; (c) hollow nanochanneled silica particle.

Thin films of PSBM were prepared by spin-coating a PSBM solution in THF onto precleaned silicon substrates and followed by drying in vacuum at room temperature for 1 day. The thin films were subjected to synchrotron XR analysis. A representative of the measured XR profiles was shown in Fig. S2.† The XR analysis found that the PSBM in films has an electron density ρ_e of 317.97 nm^{-3}. Taking into account the chemical composition determined above, the PSBM polymer

was estimated to have a mass density d_{PSBM} of 0.986 g/cm^3 from the ρ_e value. In addition, the TGA analysis found that the PSBM particle starts thermal degradation around 325 °C (= T_d) and completely degrades around 450 °C, as shown in Fig. 3. This result indicates that the PSBM particle is thermally stable up to around 325 °C in nitrogen atmosphere.

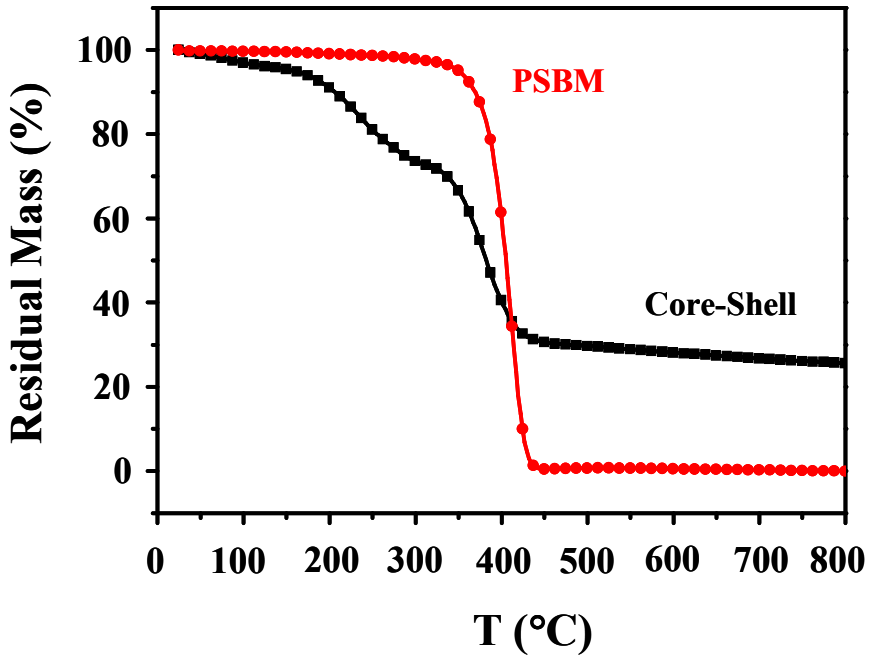

Fig. 3 TGA thermograms of PSBM particle and its core-silica precursor/CTAB shell particle. The measurements were conducted at a rate of 10.0 °C/min under nitrogen atmosphere.

The PSBM particles were further examined in aspect of morphology and size using SEM, SXS and GIXS analyses. The SEM image showed in a qualitative manner that the synthesized PSBM particles are quite uniform in size (Fig. 4a). To obtain more information on their size and distribution, the PSBM particles were further examined by synchrotron SXS and GIXS analyses. Fig. 4b shows a representative 2D grazing incidence wide angle X-ray scattering (GIWAXS) pattern of the PSBM particles. The GIWAXS pattern reveals a typical hallow ring at 13.64° (0.47 nm *d*-spacing), confirming that the PSBM particle is amorphous; the *d*-spacing of 0.47 nm corresponds to the mean interdistance of the polymer chains. Fig. 4c and d show a representative 2D solution small angle X-ray scattering (SAXS) pattern and its one-dimensional (1D) profile respectively, which were measured in ethanol. Fig. 4e and f display a representative 2D grazing incidence small angle

X-ray scattering (GISAXS) pattern and its 1D profile respectively, which were measured in vacuum. Both the 1D SAXS and GISAXS profiles reveal several oscillation peaks, which are a typical scattering feature from hard spheres. The scattering profiles could be satisfactorily fitted with the scattering formulas derived for a hard-sphere model with sharp interface, rather than any other structural models; the data analysis details are given in Supporting Information. The analysis results are summarized in Table 1.

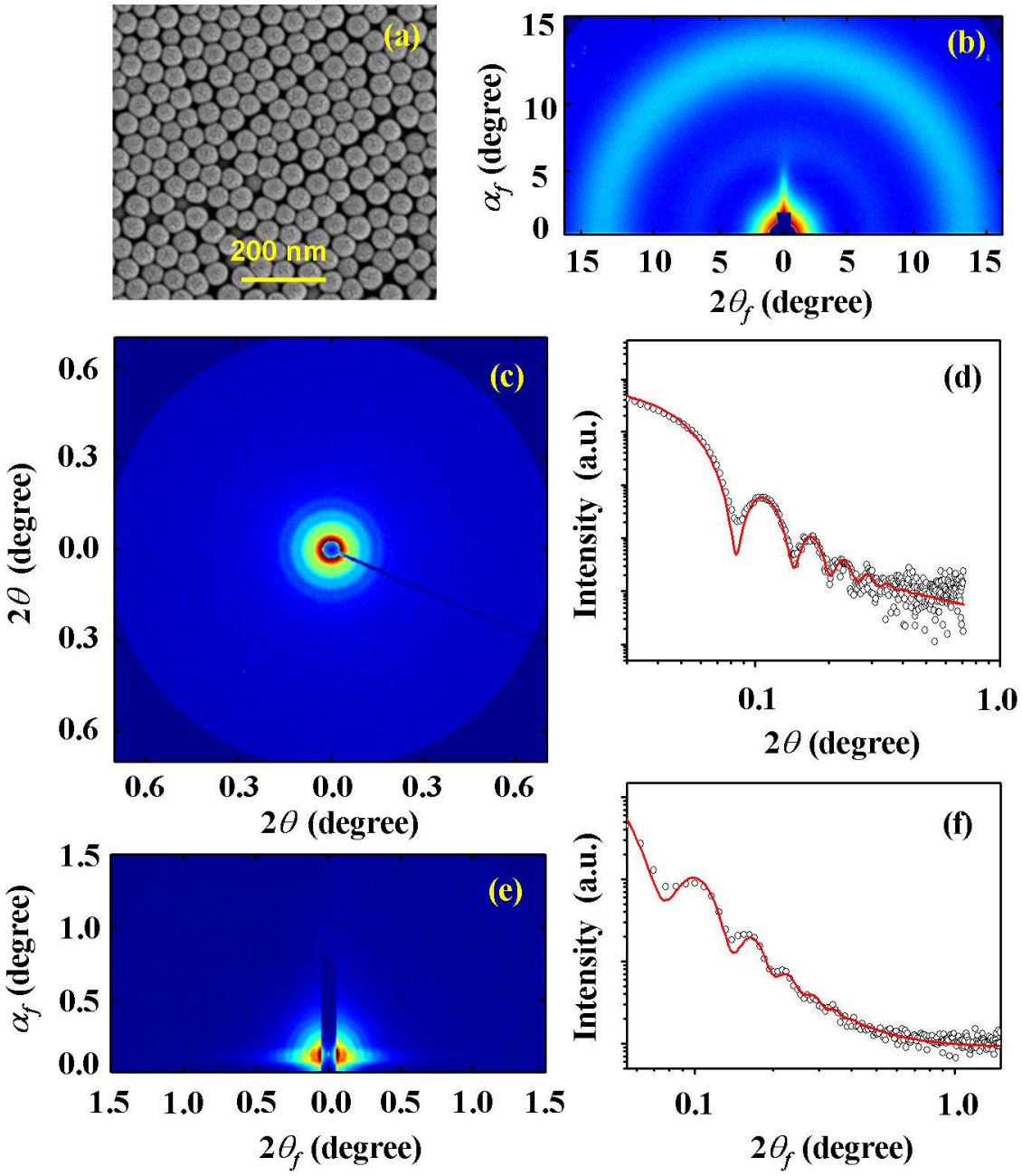

Fig. 4 PSBM particle: (a) SEM image; (b) 2D GIWXS pattern measured with a synchrotron X-ray

source with a wavelength λ of 0.1117 nm in vacuum; (c) 2D SXS pattern measured with an X-ray source of λ = 0.1100 nm in ethanol at room temperature; (d) 1D SXS profile obtained from the scattering data in (c); (e) 2D GIXS pattern measured with an X-ray source of λ = 0.1136 nm at α_i = 0.131° in vacuum at room temperature; (f) 1D GIXS profile extracted along the $2\theta_f$ direction at α_f = 0.165° from the scattering data in (e). The black symbols are the measured data; the red solid lines were obtained by fitting the data using the hard sphere model.

Table 1 Structure parameters of the PSBM, core–shell and hollow nanochanneled-silica particles

Particle sample	Method	R_o [a] (nm)	σ_R [b] (nm)	N_{agg} [c]	R_c [d] (nm)	t_s [e] (nm)	r_o [f] (nm)	σ_r [g] (nm)	ℓ_o [h] (nm)	σ_ℓ [i] (nm)	ϕ [j] (%)	$d_{c\text{-}c}$ [k] (nm)	t_w [l] (nm)	Porosity (vol%)		
														Core [m]	Shell [n]	Total [o]
PSBM	SXS	54.00	0.05	7558												
	GIXS	54.80	0.05	7899												
Core-shell	SXS	74.90	0.05		55.80	19.10	- [p]	-	-	-	-	-	-			
	GIXS	75.20	0.05		55.60	19.60	1.72	0.07	6.25	0.05	46	4.83	1.39			
Hollow core-porous shell	SXS	63.10	0.05		46.30	16.80	-	-	-	-	-	-	-			
	GIXS	63.80	0.02		47.10	16.70	1.62	0.05	6.10	0.05	45	4.60	1.36	40.2	26.9	67.1

[a] Radius of spherical particle at the peak maximum of the overall radius distribution. [b] Width in the overall radius distribution. [c] Agegation number of the polymer chains in the PSBM particle, which was estimated from the molecular weight and density of the polymer and the volume of the nanoparticle. [d] Radius of spherical core. [e] Thickness of shell (= $R_o - R_c$). [f] Radius of cylinder at the peak maximum of the cylinder radius distribution. [g] Width in the cylinder radius distribution. [h] Length of cylinder at the peak maximum of the cylinder length distribution. [i] Width in the cylinder length distribution. [j] Volume fraction of cylinders in the shell. [k] Center-to-center distance of closely neighbored two cylinders. [l] Thickness of the wall shared by the closely neighbored two cylinders. [m] Porosity of the core part in the hollow core–nanochanneled shell particle. [n] Porosity of the shell part in the hollow core–nanochanneled shell particle. [o] Total porosity of the hollow core–nanochanneled shell particle. [p] Could not be determined.

These X-ray scattering analyses found that the PSBM particles are spherical with a radius R_o of 54.00–54.80 nm and a narrow distribution width σ_R of 0.05 nm. Each nanoparticle could further be estimated to consist of 7558–7899 PSBM polymer chains (= N_{agg}, aggregation number) from the nanoparticle volume and the polymer's molecular weight and mass density. These results and analyses together confirm that sharp-surfaced amorphous PSBM nanospheres were successfully synthesized with an almost monodisperse size distribution (as indicated by the small σ_R), without any bridging flocculation and secondary nucleation, by the surfactant-free emulsion copolymerization. The absence of any bridging flocculation and secondary nucleation might be due to the clean and smooth surfaces of the PSBM nanospheres, as well as to their positively charged surfaces that were derived from the ionogenic MOTAC comonomer units and the cationic part of the AIBA initiator.

In the second stage, the positively charged PSBM nanosphere was used as a template in the

formation of the composite shell structure consisting of silica and CTAB self-assemblies. The synthesis of the shell phase with a mesoscopic ordering was carried out using a templating CTAB surfactant, inorganic precursors and reaction media often with the addition of a catalyst. In this stage, the hydrophilic part of the surfactants is associated with the surrounding inorganic precursors to form a supramolecular organic-inorganic self-assembly by adjusting the charge densities of the surfactant species and the inorganic species under the acidic or basic reaction conditions. Since the concentration of the CTAB surfactant in the synthesis solution is less than what is needed to form lyotropic micellar phases, the cooperative, dynamic mechanism has been suggested instead. In this approach, the organic surfactant molecules are associated with the inorganic species in the reaction solutions. The self-organization of the organic-inorganic assembly in two-dimensional lattices is gradually acquired during the condensation of the inorganic species. The growth of the shell phase with a mesoscopic ordering onto the positively-charged surfaces of the PSBM nanospheres was carried out by the consecutive precipitation of both the oppositely-charged, hydrolyzed silica precursors and the CTAB surfactant. The obtained core–shell particles were characterized by NMR and IR spectroscopies. ^{1}H NMR (500MHz, $CDCl_3$, δ (ppm)): 6.90–7.20 (br, 26H, aromatic proton), 6.31–6.78 (br, 21H, aromatic proton), 3.29–3.53 (br, 9H, -N(CH_3)$_3$), 1.04–2.26 (br, 56H, backbone), 0.80–0.94 (br, 7H, methyl group of BA) (Fig. 1c). The ^{1}H NMR spectrum appeared similar to that of the PSBM polymer. However, the core-shell particle particularly showed stronger chemical shift at 3.29–3.53 ppm; the integral of the chemical shift was 3.94 with respect to that of BA unit, which was higher than that (2.60) of the PSBM core itself. This enhanced chemical shift was attributed to the contribution of -N(CH_3)$_3$ groups in the CTAB surfactant assemblies associated into the silica composite shell, in addition to -N(CH_3)$_3$ groups in the MOTAC units of PSBM core. The core-shell particle revealed strong stretching vibration peaks of Si-O-C, Si-O and C-O bonds over the range 950 to 1250 cm^{-1} in the IR spectrum, as shown in Fig. 2b. These results collectively confirm that the shell part was successfully built up of silica precursor and CTAB surfactants onto the PSBM nanoparticle template.

The synthesized core-shell particles were further investigated by SEM, TEM, SXS, and GIXS. The core–shell particles were clearly shown to be spherical by SEM and TEM (Fig. 5a and b). The spherical shape of these particles was also confirmed by SXS and GIXS (Fig. 5c-g; Fig. S3 and S4[†]).

The 1D SXS profile could be satisfactorily fitted with the scattering formula derived for a core–shell sphere model (Fig. 5d; see Supporting Information for the scattering formula). In comparison, the 1D GIXS profile could be satisfactorily fitted with the GIXS formula derived for a core–shell sphere model in which the shell is composed of the CTAB surfactant cylinders and the silica precursor matrix (Fig. 5g); the derivation of the GIXS formula is given in the Supporting Information. The obtained structural parameters are listed in Table 1.

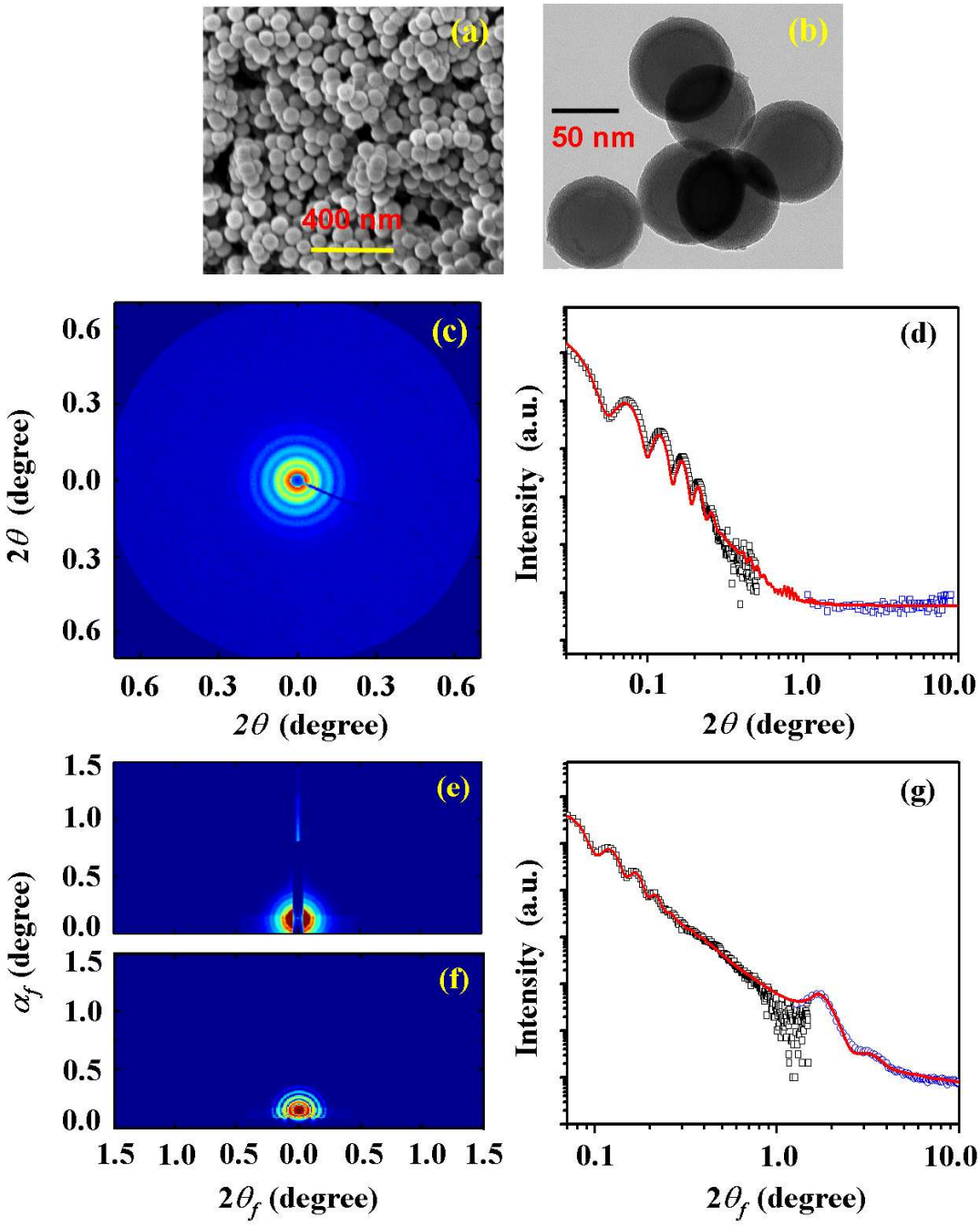

Fig. 5 Core–shell particle composed of PSBM core and surfactant/silica precursor composite shell: (a) SEM image; (b) TEM image; (c) 2D SXS pattern measured with an X-ray source of λ = 0.1100 nm in ethanol at room temperature; (d) 1D SXS profile obtained from the scattering data in (c) and Fig. S3† where the black and blue symbols are the measured data and the red solid line was obtained by fitting the data using the hard core-shell sphere model; (e) 2D GIXS pattern measured with an X-ray source of λ = 0.1180 nm at α_i = 0.140° in vacuum at room temperature; (f) 2D GIXS image reconstructed from the structural parameters determined by the quantitative analysis of the data in (e); (g) 1D GIXS profile extracted along the $2\theta_f$ direction at α_f = 0.163° from the scattering data in (e) and Fig. S4† where the black and blue symbols are the measured data and the red solid line was obtained by fitting the data using the GIXS formula derived with the hard core-shell sphere model in which the shell contains cylindrical surfactant domains.

Both the SXS and GIXS analyses gave almost the same values for the dimensions (overall size, core radius, and shell thickness) of the core-shell particles. The overall radius R_o of the core-shell particles is 74.90–75.20 nm and its σ_R is very small (0.05–0.05 nm). The core radius R_c is 55.60–55.80 nm, which is comparable to the radius of the PSBM nanosphere template. The shell thickness t_s (= R_o − R_c) is 19.10–19.60 nm. Remarkably, only the GIXS analysis could further provide structural details on the shell part, which is the first successful quantitative characterization of the shell part in the field of core–shell nanoparticles. The shell was found to consist of cylindrical domains of the surfactant CTAB molecules in the silica precursor matrix. The cylindrical surfactant domains have a radius r_o of 1.72 nm with a distribution width σ_r of 0.07 nm, a length ℓ_o of 6.25 nm with a distribution width σ_ℓ of 0.05 nm, and a volume fraction ϕ of 46% with respect to the volume of the shell. Furthermore, the GIXS analysis found that the surfactant cylinders in the shell are positioned mainly along the radial direction of the core–shell sphere. Taking this fact into account, from the structural parameters, the center-to-center distance $d_{c\text{-}c}$ of closely neighbored cylinders, as well as the thickness t_w of the well shared by the closely neighbored two cylinders was additionally estimated. The $d_{c\text{-}c}$ value is 4.83 nm, which is larger than the diameter (2 r_o = 3.44 nm) of the CTAB cylinder. The t_w value is only 1.39 nm, which is smaller than the radius (r_o = 1.72 nm) of the cylinder and further much smaller than the diameter of the cylinder. The length ℓ_o of the cylinders, however, is about 3 times less than the thickness t_s of the shell; namely, $t_s \approx 3\,\ell_o$. Taking this into account along with the relation of $t_w \ll 2\ r_o < d_{c\text{-}c}$, the structural parameters of the surfactant cylinders collectively inform that the radially-oriented surfactant cylinders were laterally packed together without any regular order and further stacked along the radial direction of the core–shell nanoparticle, forming a multilayer structure (i.e., a three-layer structure) where the cylinders between the stacked layers were interconnected with a certain degree of positional disorder in a direction parallel to the surface of the core part. Overall, these analysis results indicate that the individual PSBM nanospheres are effective templates for the formation of a well-defined shell structure composed of the surfactant cylinder domains and the silica precursor matrix. Using the structural parameters in Table 1, 2D GIXS images were reconstructed. The reconstructed scattering image is in good agreement with the experimental GIXS pattern, as shown in Fig. 5e and f.

Such a well-defined core–shell nanosphere might result from the successful, controlled deposition and growth of a surfactant/silica composite shell onto the surface of the PSBM nanosphere template as follows. The TEOS monomer undergoes a sol reaction (i.e., hydrolysis polymerization) with the aid of a base catalyst. During the polymerization, the growing silica precursors reveal negative charges. The negatively charged silica precursors can favorably interact with the positively charged surfaces of the PSBM nanosphere templates as well as the positively charged CTAB surfactant molecules via electrostatic interactions. Due to the favorable electrostatic interaction, the silica precursors can easily anchor to the surface of the PSBM nanosphere templates. During this anchoring, the CTAB surfactant may help prevent coagulation of the individual template particles. The anchored silica precursors can then continue their growth and association with the CTAB surfactant molecules. The associated surfactant molecules can further undergo cooperative silicatropic self-assembly because of their amphiphilic nature (i.e., positively-charged head and nonpolar cetyl tail), forming the cylindrical surfactant domains in the silica precursor phase. These consecutive processes ultimately produce the well-defined silica precursor shell composited with the self-assembled CTAB cylinder domains onto the PSBM nanosphere nanotemplate.

The core-shell nanoparticles were further examined by TGA, as were the PSBM nanospheres. The core-shell particles exhibit a three-step weight loss (Fig. 3). In comparison, the PSBM particles undergo a single step weight loss between 325 and 450 °C, and leave no char. Note that silica precursor (i.e., prepolymer) is known to undergo a secondary condensation reaction between room temperature and about 150 °C, forming a more densely networked silica polymer and producing volatile byproducts (alcohol and water).[28] Also note that CTAB surfactant is known to have a flash point of 224 °C.[29] Taking these considerations into account, about 8% of the weight loss of the core-shell particles in the first step between 40 and 175 °C can be attributed mainly to the removal of residual solvent as well as the byproducts (ethanol and water) of the secondary condensation reaction of the silica prepolymers in the shell. About 21% of the weight loss in the second step (175–325 °C) results mainly from the removal of the self-assembled CTAB surfactant molecules in the shell, whereas about 41% of the weight loss in the third step (325–450 °C) is caused mainly by the thermal degradation of the PSBM nanosphere core template. These TGA results collectively indicate that the organic polymer core as well as the self-assembled organic surfactant cylinder

domains in the shell can be completely removed by thermal treatment at a temperature of 450 °C or higher.

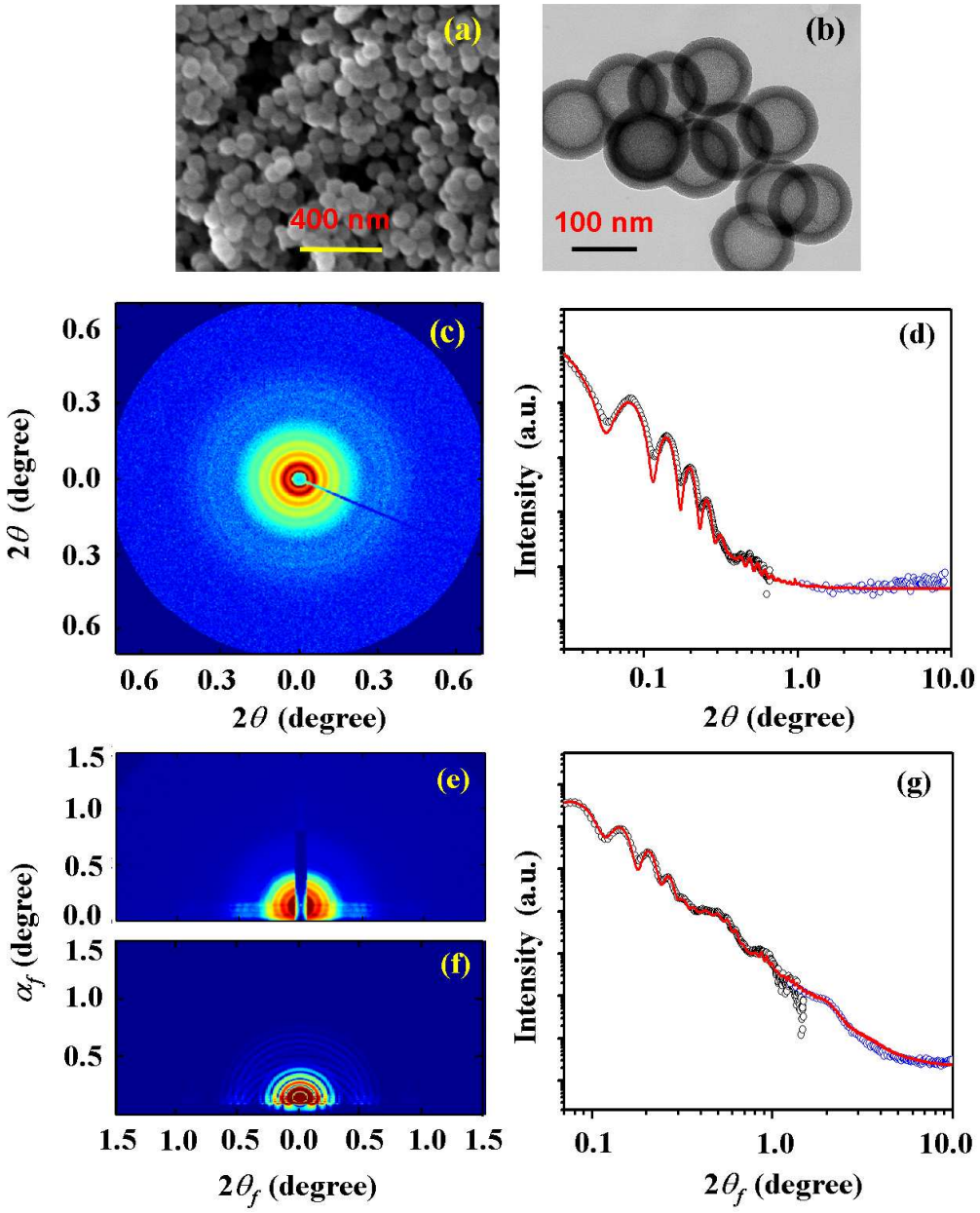

Fig. 6 Hollow nanochanneled-silica particle: (a) SEM image; (b) TEM image; (c) 2D SXS pattern measured with an X-ray source of λ = 0.1100 nm in ethanol at room temperature; (d) 1D SXS profile obtained from the scattering data in (c) and Fig. S5† where the black and blue symbols are the measured data and the red solid line was obtained by fitting the data using the hard core-shell sphere model; (e) 2D GIXS pattern measured with α_i = 0.140° in vacuum at room temperature; (f) 2D GIXS image reconstructed from the structural parameters determined by the quantitative analysis of the data in (e); (g) 1D GIXS profile extracted along the $2\theta_f$ direction at α_f = 0.163° from the scattering data in (e) and Fig. S6† where the black and blue symbols are the measured data and the red solid line was obtained by fitting the data using the GIXS formula derived with the hard

core-shell sphere model in which the shell contains cylindrical pores.

Using the TGA results and analysis as guidance, in the final step the core–shell particles were further selectively calcined at 600 °C under nitrogen atmosphere for 8 h in order to convert them to hollow mesoporous-silica particles. During calcination, the hydrolyzed silica precursors were then thermally condensed and held together by a network of -Si-O- bonds through a solid rearrangement reaction. These sol particles tend to coalesce to form a three-dimensional network, the gel. Because a low concentration of the silica precursors was used to make the sol, its gelation proceeded slowly in a solution. The selectively calcined particles were examined by IR spectroscopy. In the calcined particles, vibrational characteristics of the PSBM core template and the cylindrical CTAB domains disappeared while the vibrational Si-O characteristics became stronger, as shown in Fig. 2c.

The SEM and TEM analyses confirmed that the overall spherical shape of the core-shell particle was well retained without collapse during the thermal calcination process (Fig. 6a-b). Moreover, the shell became more clearly distinguishable from the core after the calcination process. The spherical characteristics were again confirmed in the SXS and GIXS analyses (Fig. 6c-g; Fig. S5 and S6[†]). The 1D SXS profile in Fig. 6d could be satisfactorily fitted with the scattering formula derived for a simple core-shell sphere model. On the other hand, the GIXS profile in Fig. 6g could be satisfactorily fitted with the GIXS formula derived for another core-shell sphere model in which the shell is composed of cylindrical pores and silica matrix. The obtained structural parameters are listed in Table 1. Both the SXS and GIXS analyses provided almost the same values for the dimensions (overall size, core radius, and shell thickness) of the spherical particle consisting of a hollow core and mesoporous shell: R_o = 63.10~63.80 nm (σ_R = 0.02~0.05 nm), R_c = 46.30~47.10 nm, and t_s = 16.70~16.80 nm. Furthermore, the GIXS analysis is the first case providing the structural details on the mesoporous shell: the cylindrical pores have r_o = 1.62 nm (σ_r = 0.05 nm), ℓ_o = 6.10 nm (σ_ℓ = 0.05 nm), and ϕ = 45% (i.e., the porosity with respect to the shell volume). The GIXS analysis further confirms that the cylindrical pores generated in the shell are preferentially oriented along the radial direction of the hollow silica sphere, as observed for the surfactant cylinders in the shell of the core-shell sphere particle. Taking this fact into account, it is further estimated from the structural parameters that $d_{c\text{-}c}$ = 4.60 nm (which is larger than 2 r_o (3.24 nm)) and t_w = 1.36 nm (which is much smaller than 2r_o). These results together indicate that the core-shell particle successfully underwent the selective calcination process with little change in

dimensions and, as a result, the thermally sacrificed PSBM core and self-assembled CTAB surfactant cylinder domains in the shell were completely removed, producing a well-defined hollow nanochanneled-silica sphere particle. Using the structural parameters in Table 1, 2D GIXS image was reconstructed. The reconstructed scattering image agrees well with the experimental GIXS pattern (Fig. 6e and f).

The results of GIXS analysis further inform that the calcination process caused a small decrease in the dimensions of the particle, including of the core and shell as well as in the cylindrical domains in the shell: The R_o value was reduced by 15.2–15.8%, the R_c reduced by 15.2–17.0%, and the t_s reduced by 12.0–14.8%; the r_o and ℓ_o were reduced by 5.8% and 2.4% respectively, and the ϕ reduced by 2.2%. In particular, the reduction in the t_s is relatively severe, compared to those in the r_o and ℓ_o. These results indicate that shrinkage was taken place nonuniformly between the cylindrical domains and the shell matrix during the selective calcination process. Considering the TGA results above, the relatively high shrinkage of the shell matrix might be attributed to the losses of the residual solvent and the ethanol and water byproducts of the secondary condensation reaction of the silica precursors during the calcination process. The chemical network formations by the secondary condensation make additional contribution to the shrinkage. In contrast, the observation of the relatively very small shrinkage in the cylindrical domains suggests that the CTAB cylinder domains retained their dimension very well until the thermal degradation despite their matrix, namely the silica precursor matrix, underwent a certain level of shrinkage due to the mass losses as well as a densification based on the network formations. These imbalanced shrinkages may cause a kink on the interconnected parts of the radially-aligned cylindrical domains, producing the radially-aligned hollow cylinders interconnected with a kink inside the shell. Such radially-aligned hollow cylinders interconnected with a kink are evident in the relation of t_s and ℓ_o, together with another relation $t_w << 2\ r_o < d_{c\text{-}c}$: $t_s < 3\ \ell_o$, which is far from the relation $t_s \approx 3\ \ell_o$ observed for the core–shell nanoparticle before the selective calcination. From the relation $t_s < 3\ \ell_o$, the kink angle is estimated to be ca. 24°, which corresponds to the angle between the interconnected cylindrical pores. It turns out that the radially-oriented, interconnected cylindrical pores in the shell can play as open nanochannels between the hollow core and the outer space.

As described above, the SXS technique in this study was found to yield a low-resolution

structural analysis compared to the GIXS technique. The relatively poor resolution of SXS was indicated by the lack of any discernible scattering signals in the high-angle region of >1.0°. Such a lack of discernible scattering signals in the high-angle region indicates that there is relatively low contrast in the electron density between the surfactant domain and silica phase of the core-shell particles in ethanol solvent, as well as between the ethanol-filled nanopore and the silica phase of the hollow nanochanneled-silica particles in ethanol. In contrast, the GIXS technique yielded higher resolution data due to the relatively high contrast in electron density between the cylindrical surfactant domain and silica phase of the core-shell particles in vacuum, as well as between the nanochannels and silica phase of the hollow mesoporous-silica particles in vacuum.

Based on the SEM, TEM, SXS, and GIXS analysis results, structural models have been proposed for the core-shell particle and its hollow nanochanneled-silica particle, as shown in Fig. 7.

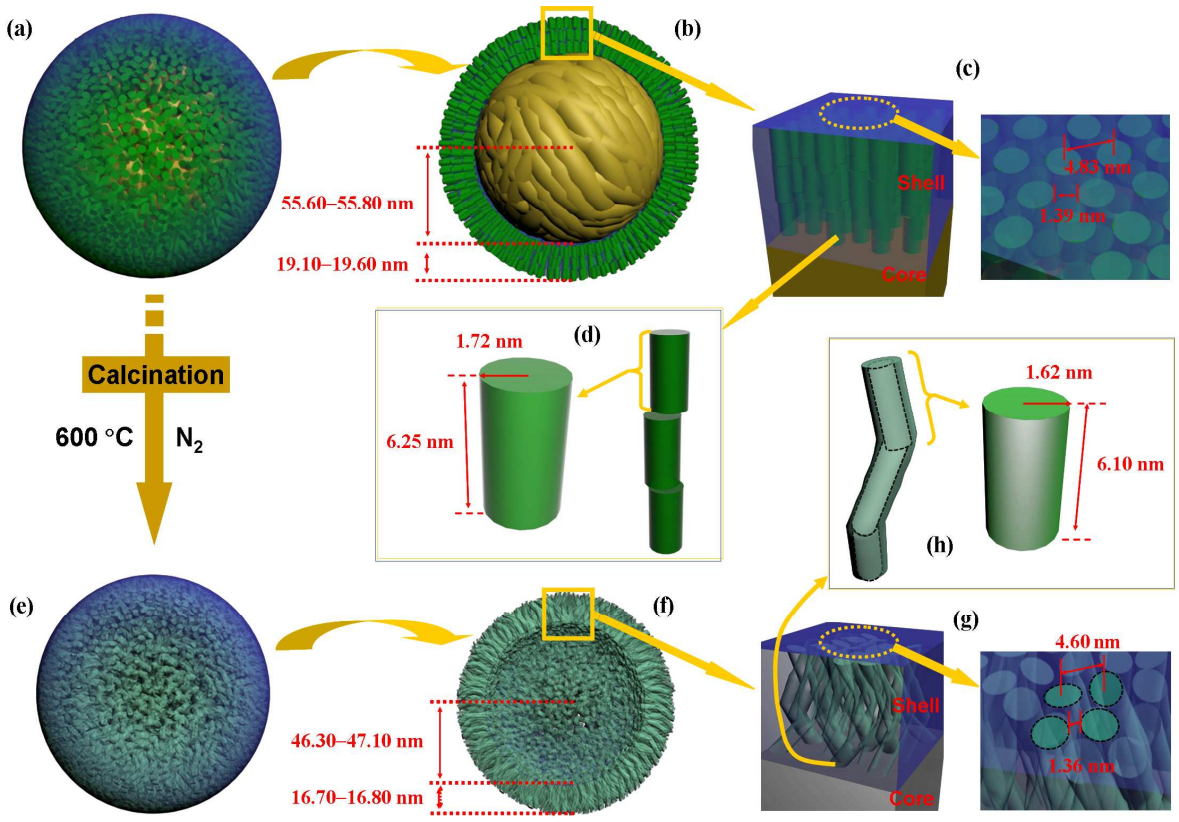

Fig. 7 Schematic structural representations of nanoparticles, which were proposed from the SEM, TEM, SXS and GIXS analysis results: (a) core–shell particle where the self-assembled surfactant cylinder domains were developed in the shell; (b) hemispherical view of the core-shell particle in (a); (c,d) radially-aligned cylindrical surfactant domains interconnected with a certain degree of positional disorder in a direction parallel to the surface of the core part and their lateral packing, forming a three-layer structure; (e) hollow nanochanneled-silica particle where the hollow core was imprinted by the selective calcination of the PSBM core while the cylindrical pores were imprinted

in the shell by the selective calcination of the cylindrical surfactant domains; (f) hemispherical view of the hollow nanochanneled-silica particle in (e); (g,h) radially-aligned cylindrical pores interconnected with a kink in the shell and their lateral packing, forming open nanochannels to connect the hollow core and the outer space.

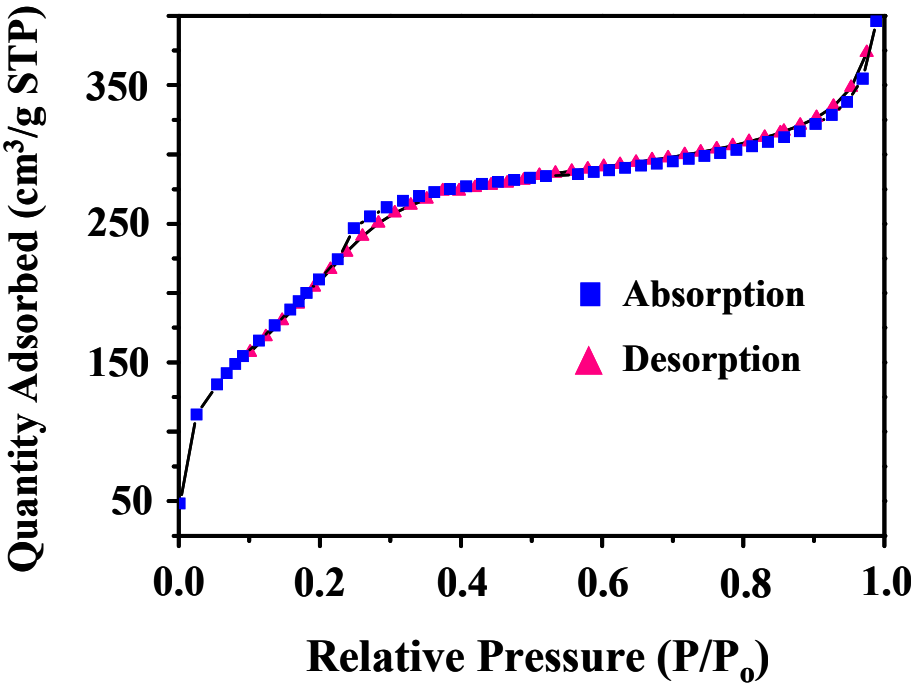

Fig. 8 N_2 adsorption-desorption isotherms of the compounds of the hollow nanochanneled-silica nanoparticle.

In addition, the hollow nanochanneled-silica particles were examined by Brunauer-Emmet-Teller (BET) analysis. Fig. 8 shows representative N_2 adsorption-desorption isotherms measured for the hollow nanochanneled-silica particles. The isotherm reveals a type-IV adsorption behavior with H1 hysteresis and a N_2 BET surface area of 807.4 m^2/g. From the BET analysis, the mean pore size was estimated to be 3.03 nm, which is comparable with the average diameter (3.24 nm) of the cylindrical pores in the shell determined by the GIXS analysis.

The obtained hollow nanochanneled-silica sphere particle was found to have a total porosity of 67.1%, with its hollow core having a volume of 4.38×10^5 nm^3 (40.2% porosity with respect to the overall volume of the hollow nanochanneled-silica particle) and the nanochanneled-shell having

a total cylindrical pore volume of 2.92×10^5 nm^3 (26.9% porosity with respect to the overall volume of the hollow nanochanneled-silica particle) (Table 1). Due to the combination of such relatively large volumes of the hollow core and of the cylindrical nanopores in the mesoporous shell, the hollow nanochanneled-silica sphere particle may find potential applications in various fields including advanced drug and gene delivery and photoelectronics.

CONCLUSIONS

This study demonstrated for the first time the synthesis and structural details of monodisperse, well-defined hollow nanochanneled-silica nanosphere particles. Well defined, positively charged PSBM nanosphere particles with clean, smooth surfaces were successfully synthesized by surfactant-free emulsion copolymerization and then used as core templates for the production of core-shell nanoparticles. A uniform, thin surfactant/silica composite shell was deposited onto the PSBM particles, without coagulation, by hydrolysis polycondensation of TEOS associated with CTAB surfactant. In particular, such high quality shell formation was successfully carried out with the aid of charge density matching (i.e., favorable electrostatic interaction) between the positively charged template and the negatively charged silica precursors associated with the surfactant. During the formation of the shell, the surfactant molecules were self-assembled, forming cylindrical nanodomains. Both the polymeric core and the surfactant cylinder domains in the shell were selectively removed from the core-shell nanoparticle without collapse by calcination, producing the hollow nanochanneled-silica nanosphere. The comprehensive analyses collectively confirmed that the hollow mesoporous-silica sphere particle is monodisperse and structurally well defined, with the hollow core and the shell composed of cylindrical nanochannels that permit facile accessibility to the hollow interior space. Due to the unique structure and the facile accessibility to the hollow interior space, the monodisperse, well-defined hollow nanochanneled-silica sphere of our study has potential applicability in various fields including drug and gene delivery, cosmetics, catalysis, rechargeable battery research and development, sensors, selective separation, gas adsorption,

hydrogen production and storage, photonics, and photovoltaics.

Acknowledgements

This study was supported by the National Research Foundation (NRF) of Korea (NRF-2009-C1AAA001-2009-0093204 and Doyak Program 2011-0028678), Inha University, and the Ministry of Science, ICT & Future Planning (MSIP) and the Ministry of Education (BK21 Plus Program and Global Excel Program). The synchrotron X-ray scattering measurements at the Pohang Accelerator Laboratory were supported by MSIP and POSCO Company and POSTECH Foundation.

References

1 Y. Lu, H. Fan, A. Stump, T. L. Ward, T. Rieker and C. J. Brinker, *Nature*, 1999, **398**, 223-226.

2 G. V. Rama Rao, G. P. Lopez, J. Bravo, H. Pham, A. K. Datye, H. Xu and T. L. Ward, *Adv. Mater*., 2002, **14**, 1301-1304.

3 R. Schiller, C. K. Weiss, J. Geserick, N. Hüsing and K. Landfester, *Chem. Mater.*, 2009, **21**, 5088-5098.

4 X. W. Lou, L. A. Archer and Z. Yang, *Adv. Mater.*, 2008, **20**, 3987-4019.

5 G.-D. Fua, G. L. Li, K. G. Neoh and E. T. Kang, *Prog. Polym. Sci*., 2011, **36**, 127-167.

6 W. Meier, *Chem. Soc. Rev.*, 2000, **29**, 295-303.

7 F. Caruso, R. A. Caruso and H. Mohwald, *Science*, 1998, **282**, 1111-1114.

8 T. H. Kim, K. H. Lee and Y. K. Kwon, *J. Colloid. Interface. Sci*., 2006, **304**, 370-377.

9 J. Ge, Q. Zhang, T. Zhang and Y. Yin, *Angew. Chem*., 2008, **120**, 9056-9060.

10 C. C. Striemer, T. G. Gaborski, J. L. McGrath and P. M. Fauchet, *Nature*, 2007, **445**, 749-753.

11 B. Coasne and R. J.-M. Pellenq, *J. Chem. Phys*. **2004**, *120*, 2913-2922.

12 Y. Chen, H. Chen, D. Zeng, Y. Tian, F. Chen, J. Feng and J. Shi, *ACS Nano*, 2010, **4**, 6001-6003.

13 J. Zhang, Z.-F. Yuan, Y. Wang, W.-H. Chen, G.-F. Luo, S.-X. Cheng, R.-X. Zhuo and X.-Z. Zhang, *J. Am. Chem. Soc.*, 2013, **135**, 5068-5073.

14 Z. Zhao, H. Meng, N. Wang, M. J. Donovan, T. Fu, M. You, Z. Chen, X. Zhang and W. Tan, *Angew. Chem. Int. Ed.*, 2013, **52**, 1-6.

15 Y. Chen, H. Chen, D. Zeng, Y. Tian, F. Chen, J. Feng and J. Shi, *ACS Nano*, 2010, **4**, 6001-6013.

16 W. Li, X. Sha, W. Dong and Z. Wang, *Chem. Commun*., 2002, **20**, 2434-2435.

17 S. Colodrero, M. Ocaña, A. R. González-Elipe and H.Míguez, *Langmuir*, 2008, **24**, 9135-9139.

18 G. Qi, Y. Wang, L. Estevez, A. K. Switzer, X. Duan, X. Yang and E. P. Giannelis, *Chem. Mater.*, 2010, **22**, 2693-2695.

19 S. R. Shin, K. S. Jin, C. K. Lee, S. I. Kim, G. M. Spinks, I. So, J.-H. Jeon, T. M. Kang, J. Y. Mun, S.-S. Han, M. Ree and S. J. Kim, *Adv. Mater.*, 2009, **21**, 1907-1910.

20 M. Kim, Y. Rho, K. S. Jin, B. Ahn, S. Jung, H. Kim and M. Ree, *Biomacromolecules*, 2011, **12**, 1629-1640.

21 K. Heo, Y. Y. Kim, Y. Kitazawa, M. Kim, K. S. Jin, T. Yamamoto and M. Ree, *ACS Macro Lett.*, 2014, **3**, 233-239.

22 Y. Rho, B. Ahn, J. Yoon and M. Ree, *J. Appl. Crystallogr.*, 2013, **46**, 466-475.

23 Y. Rho, C. Kim, T. Higashihara, S. Jin, J. Jung, T. J. Shin, A. Hirao and M. Ree, *ACS Macro Lett.*, 2013, **2**, 849-855.

24 K. Kim, Y. Y. Kim, S. Park, Y.-G. Ko, Y. Rho, W. Kwon, T. J. Shin, J. Kim and M. Ree, *Macromolecules*, 2014, **47**, 4397-4407.

25 M. Ree, *Macromol. Rapid Commun.*, 2014, **35**, 930-959.

26 B.-J. Park, S.-Y. Rah, Y.-J. Park and K.-B. Lee, *Rev. Sci. Instrum.*, 1995, **66**, 1722-1724.

27 J. Bolze, M. Ree, H. S. Youn, S. H. Chu and K. Char, *Langmuir*, 2001, **17**, 6683-6691.

28 W. Oh, Y.-t. Hwang, Y. H. Park, M. Ree, S.-H. Chu, K. Char, J. K. Lee and S. Y. Kim, *Polymer*, 2003, **44**, 2519-2527.

29 Material Safety Data Sheet, Sigma-Aldrich, 2014.

Graphic TOC

Well-defined hollow nanochanneled-silica nanosphere prepared with aids of sacrificial copolymer nanosphere and surfactant nanocylinders

Young Yong Kim, Bora Hwang, Sungjin Song, Brian J. Ree, Yongjin Kim, Seo Yeon Cho, Kyuyoung Heo, Yong Ku Kwon and Moonhor Ree